Long-duration 3D single-molecule tracking maps transport landscapes within tau condensates

Junhui Huang[1], Ran Liu[1,2], Yuxin Lin[3], Ziwei Shi[1,4,5], Yilin Tian[1,6], Shangguo Hou[1,4*]

[1] *Institute of Systems and Physical Biology, Shenzhen Bay Laboratory, Shenzhen 518132, China.*

[2] *School of Life Science and Technology, Harbin Institute of Technology, Harbin 150001, China*

[3] *Lyda Hill Department of Bioinformatics, UT Southwestern Medical Center, Dallas, TX 75390, USA*

[4] *Shenzhen Medical Academy of Research and Translation (SMART), Shenzhen 518107, China*

[5] *Westlake University, Hangzhou 310030, China*

[6] *University of Nottingham Ningbo China, Ningbo 315000, China*

Correspondence: Shangguo Hou, Shangguo.hou@szbl.ac.cn

Abstract

Biomolecular condensates are spatially heterogeneous, but most measurements either average over molecular populations or yield trajectories too short to reveal how individual molecules traverse this heterogeneity. Here, we use active-feedback three-dimensional single-molecule tracking to follow individual fluorescently labelled tau molecules continuously within reconstituted condensates for tens to more than 100 s. The resulting long trajectories reveal recurrent switching among three apparent mobility states, spatially revisited residence hotspots enriched in slow and subdiffusive motion, and restricted shell-like motion in representative boundary-associated trajectories. We further capture repeated single-molecule transfer between adjacent condensates. A representative continuous trajectory resolves inter-condensate passages lasting tens of milliseconds. The configurational free-energy difference predicted from the molecule-accessible volume ratio closely matches the occupancy-derived value, revealing a quantitative correspondence between molecular occupancy and accessible configurational space. Thus, long-

duration 3D single-molecule tracking preserves sufficient molecular history to connect heterogeneous transport, local confinement, interfacial motion, exchange kinetics, and trajectory-derived thermodynamic partitioning within the same measurement, providing a framework for reconstructing the transport and effective free-energy landscapes experienced by individual molecules in biomolecular condensates.

Introduction

Biomolecular condensates organize biochemical reactions by concentrating proteins, nucleic acids and other biomolecules without a surrounding membrane[1, 2]. They participate in transcriptional regulation, RNA metabolism, signal transduction and stress responses[3-6], and their dysregulation has been linked to neurodegeneration and cancer[7, 8]. Although condensates are frequently described as liquid-like compartments with well-mixed interiors, this approximation is increasingly incomplete. Experiments and simulations have revealed local density fluctuations, interaction networks, physicochemical gradients and regions with distinct molecular mobilities within condensates[2, 9-16]. Such heterogeneity can in principle regulate where molecules accumulate, how long they remain locally confined and how rapidly they encounter reaction partners. Understanding condensate function therefore requires not only average material properties, but also a description of how individual molecules move through these heterogeneous environments over time.

A broad range of methods has been utilized to characterize condensate material properties and internal organization[2, 9, 16-18]. However, most established measurements provide only averaged dynamic readouts. Fluorescence recovery after photobleaching (FRAP), fluorescence correlation spectroscopy and mechanical assays provide valuable information on exchange, diffusion and viscoelasticity[19-24], but they predominantly report population- or volume-averaged behavior. Super-resolution imaging and conventional single-molecule tracking alleviate ensemble averaging and have revealed nanoscale organization and heterogeneous molecular mobility in several condensate systems[10, 12, 13, 25, 26]. Recent intra-condensate single-molecule measurements, for example, identified nanoscale regions with distinct local diffusion and chemical environments in FUS condensates[12]. However, a complementary challenge remains, i.e., following the same molecule continuously in three dimensions for long enough to reveal how it revisits particular

locations, switches among mobility states, explores the phase boundary and transfers between neighboring condensates.

Long, continuous trajectories can in principle provide information beyond local mobility. A molecular trajectory records not only instantaneous displacement but also the sequence and duration of states explored by the molecule. Its temporal order identifies state switching, confinement, escape and revisitation; its spatial coordinates define the local environments and configurational space explored by the molecule; and its fractional occupancy can be related to apparent free-energy differences between trajectory-defined states. Repeated transitions can additionally reveal brief exchange pathways that are difficult to capture in population-averaged measurements. Theoretical work has likewise emphasized that phase boundaries, local trapping and nonequilibrium transport can leave characteristic signatures in single-molecule trajectories[27]. Experimentally realizing this potential remains challenging because conventional fluorescence trajectories are often short and fragmented owing to photobleaching, motion blur, and defocalization. The intrinsically three-dimensional geometry of condensates further complicates interpretation when axial motion is not measured.

Here we address this challenge using long-term three-dimensional single-molecule active real-time tracking microscopy (3D-SMART), which is previously developed for extended target-locked measurements[28-32]. We apply the approach to reconstituted condensates formed by tau, an intrinsically disordered microtubule-associated protein that can undergo phase separation in vitro, and condensation has been linked to changes in tau molecular organization and pathological-state formation[33, 34]. 3D-SMART uses active feedback to maintain a tau molecule near the excitation volume as it moves, while high-frequency periodic illumination mitigates photobleaching by allowing triplet-state relaxation[35, 36]. These features extend continuous 3D trajectory acquisition into the tens-to-hundreds-of-seconds regime at a temporal resolution of 1 ms, enabling molecular behavior to be interrogated directly from individual motion histories rather than reconstructed from many short, fragmented trajectories.

The resulting tau trajectories reveal recurrent switching among three mobility states, localized regions of prolonged residence, shell-like motion associated with condensate boundaries and direct molecular transfer between adjacent condensates. Importantly, segmentation of an inter-condensate trajectory into condensate-associated and transition states enables the extraction of

occupancy-derived free-energy differences and molecule-accessible configurational volumes. For the analyzed event, the occupancy-derived free-energy difference closely matched that predicted from the tau-accessible volume ratio, linking the observed molecular partitioning to the configurational space sampled by the tracked molecule. Together, these results establish long-duration 3D tracking as a means of linking heterogeneous molecular transport to the effective thermodynamic landscape sampled by an individual molecule. The method complements ensemble thermodynamic and exchange measurements by revealing how kinetic heterogeneity, local confinement, interfaces and partitioning are experienced within the continuous history of an individual molecule.

Results

Long-duration active-feedback tracking preserves continuous 3D histories of single tau molecules

We first established long-duration tracking of fluorescently labelled tau within reconstituted condensates. Recombinant tau was labelled with SeTau647, and condensate formation was characterized by confocal fluorescence microscopy, FRAP and turbidity measurements under the reconstitution conditions used here (**Supplementary Fig. 1–3**). For single-molecule measurements, labelled tau was diluted into a large excess of unlabeled tau to minimize simultaneous detection of multiple fluorescent molecules.

The stable, continuous single-molecule tracking capability of 3D-SMART relies on rapid molecular-position estimation and rapid active displacement compensation[28-30]. In this system, a tunable acoustic gradient (TAG) lens provides rapid axial modulation, while two-dimensional electro-optic deflectors steer the excitation beam laterally to generate a three-dimensional excitation pattern around the target molecule (**Fig. 1a**). Fluorescence photons are detected by a single-photon detector, and their arrival times are processed in real time by an FPGA to estimate the molecular position. The estimated displacement is then fed back to a nanopositioning stage to keep the molecule near the center of the excitation volume. This closed-loop target-locking strategy reduces trajectory loss caused by defocalization and therefore enables continuous long-term 3D position measurement.

Using this approach, individual tau molecules can be tracked continuously for tens to more than 100 s inside a condensate (**Fig. 1b**). Each record contains the evolving three-dimensional position and the fluorescence-intensity trace of the target along time axis. Because the photon arrival times and laser-focus positions are stored during the experiment, the trajectories can be further reconstructed at a temporal resolution of 100 μs using recursive Bayesian position estimation[37]. The resulting long, temporal continuous trajectories contain enough temporal depth for diffusion analysis, residence-time reconstruction, hotspot detection, interface mapping, the observation of single-molecule inter-condensate transfer and state-resolved thermodynamic analysis (**Fig. 1c**).

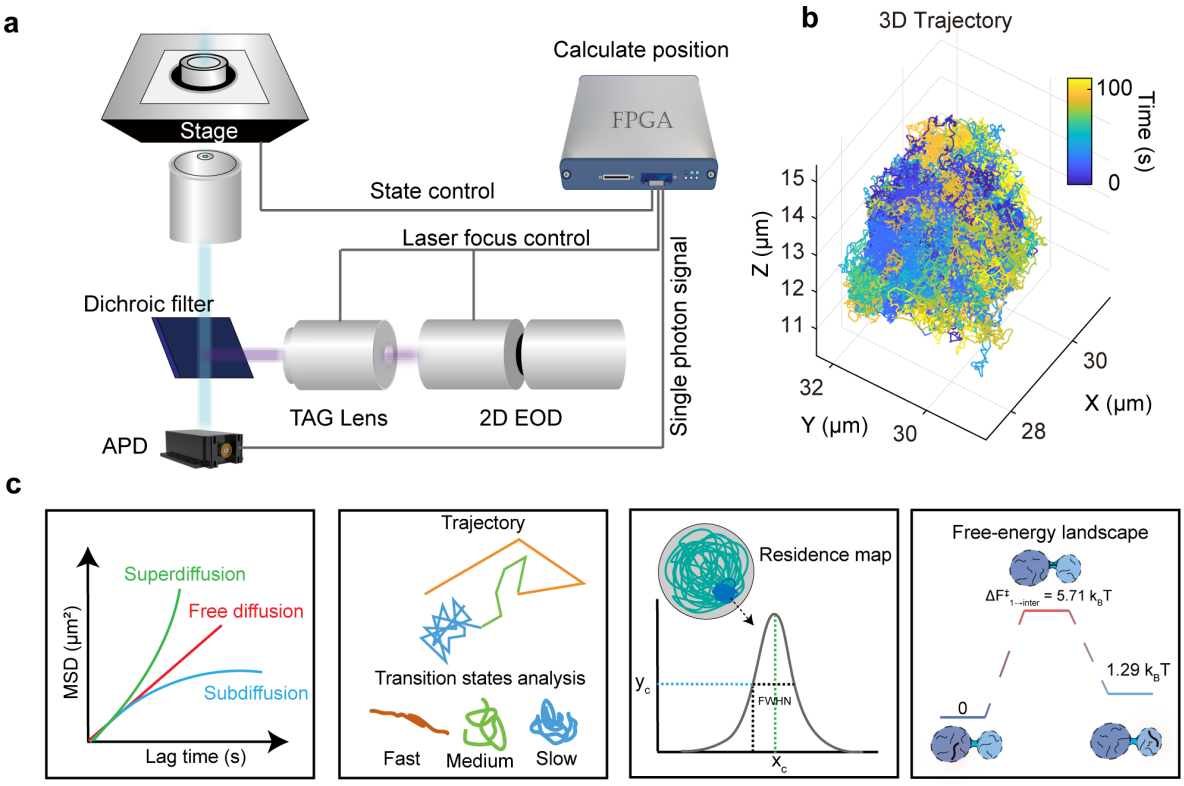

Figure 1. Long-duration 3D tracking of single tau molecules within condensates. (a) Schematic of the 3D-SMART platform. A TAG lens and two-dimensional electro-optic deflectors generate a three-dimensional excitation pattern around the tracked fluorophore. Photon arrival times are processed in real time to estimate target position, and a nanopositioning stage compensates for molecular displacement. **(b)** Representative three-dimensional trajectory of a

tau molecule moving within a condensate, color-coded by time, showing continuous tracking for more than 100 s. **(c)** Overview of trajectory analyses used to quantify local mobility, classify mobility states, reconstruct residence maps, identify localized residence hotspots, characterize boundary-associated motion, and infer apparent free-energy differences from trajectory-defined states.

Long trajectories resolve recurrent transitions among three mobility states

By continuously tracking sparsely labeled tau molecules in condensates, we resolved distinct diffusive states and observed switching between them (**Fig. 2**). **Fig. 2a** shows a representative 3D trajectory of a single tau molecule diffusing inside a condensate lasting more than 180 seconds (the x-, y- and z-position and intensity traces are shown in **Supplementary Fig. 4**). The tracked data were further reconstructed at 100-μs time precision using recursive Bayesian position estimation. Using these high-precision 3D trajectory, local diffusion parameters were calculated and classified using a hidden Markov model (HMM). We identified three diffusive states according to their apparent diffusivity: fast, medium and slow states (**Fig. 2b**). An aggregated transition matrix was also constructed from 75 analyzed trajectories (**Fig. 2c**).

The three states also differed in their diffusive character. State-specific apparent diffusion-coefficient distributions were separated, with the slow, intermediate and fast classes showing progressively increasing mobility (**Fig. 2d**). Analysis of the anomalous diffusion exponent further indicated that slow-state segments were predominantly subdiffusive, the medium state approached Brownian behavior, and the fast state was approximately Brownian under the present experimental conditions (**Fig. 2e**). Thus, individual tau molecules did not simply alternate between a freely diffusing and an immobilized population. Instead, the long trajectories resolved repeated sampling of multiple kinetic environments within the same dense phase.

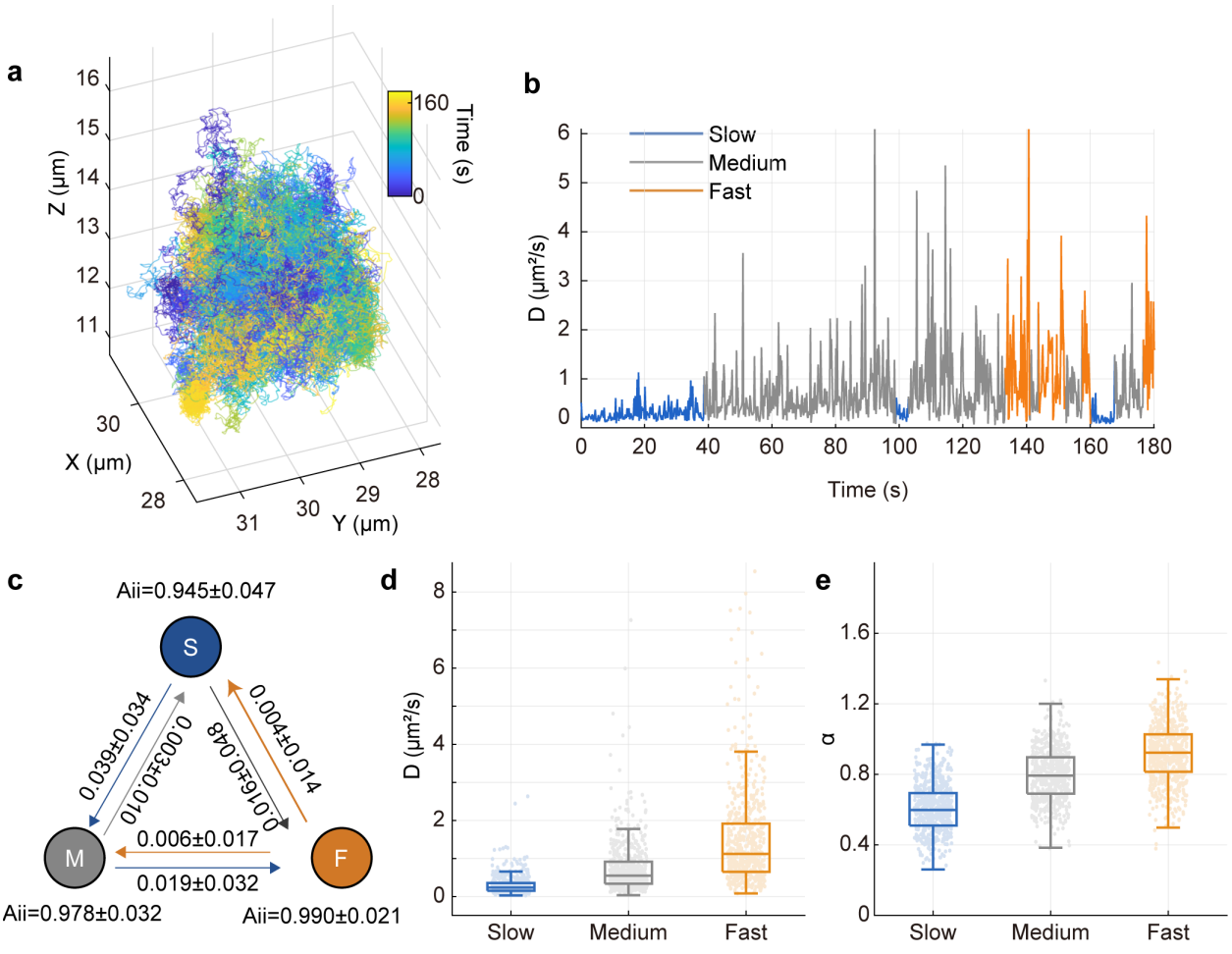

Figure 2. Long trajectories resolve three recurrent tau mobility states within condensates. (a) Representative three-dimensional tau trajectory, color-coded by time. **(b)** Time trace of the local diffusion coefficient for trajectory (**a**), with identification of diffusive states by hidden Markov model (HMM) classification, revealing three distinct states. The diffusion coefficients are 0.28 ± 0.16 μm²/s for slow-state segments, 0.74 ± 0.68 μm²/s for medium-state segments, and 1.36 ± 0.98 μm²/s for fast-state segments. **(c)** Aggregated transition matrix obtained from the HMM analysis. Number of trajectories used here is 75. **(d)** Distribution of state-specific apparent mobility parameters for the 75 analyzed trajectories. The diffusion coefficients are 0.30 ± 0.23 μm²/s for slow-state segments, 0.75 ± 0.68 μm²/s for medium-state segments, and 1.51 ± 1.33 μm²/s for fast-state segments. **(e)** Distribution of anomalous diffusion exponents for slow-, medium- and fast-state trajectory segments. The mean α is 0.609 ± 0.139 for slow-state segments, 0.80 ± 0.15 for medium-state segments, and 0.92 ± 0.16 for fast-state segments. $n = 75$ trajectories. Temporal precision of data used for (**b**-**e**): 100 μs.

Recurrent residence hotspots mark locally confining environments

We next asked whether changes in mobility were spatially organized. The long, continuous, high-precision trajectories enabled spatial reconstruction of residence time with a 30-nm pixel size, revealing pronounced heterogeneity in where tau molecules reside within a condensate (**Fig. 3a**). Rather than sampling the interior uniformly, individual molecules repeatedly revisited a limited set of localized high-residence regions, which we refer to as residence hotspots. Moreover, hotspots repeatedly appeared in the same area over time, indicating recurrent local confinement over the observation period (**Supplementary Fig. 5**). To determine whether these regions reflected reproducible molecular dynamics rather than transient density fluctuations, we calculated a coarse-grained local drift field from lagged molecular displacements along the same trajectory (**Fig. 3b**). The resulting vector field exhibited localized directional structure around high-residence regions, providing a dynamical correlate of the heterogeneous spatial occupancy.

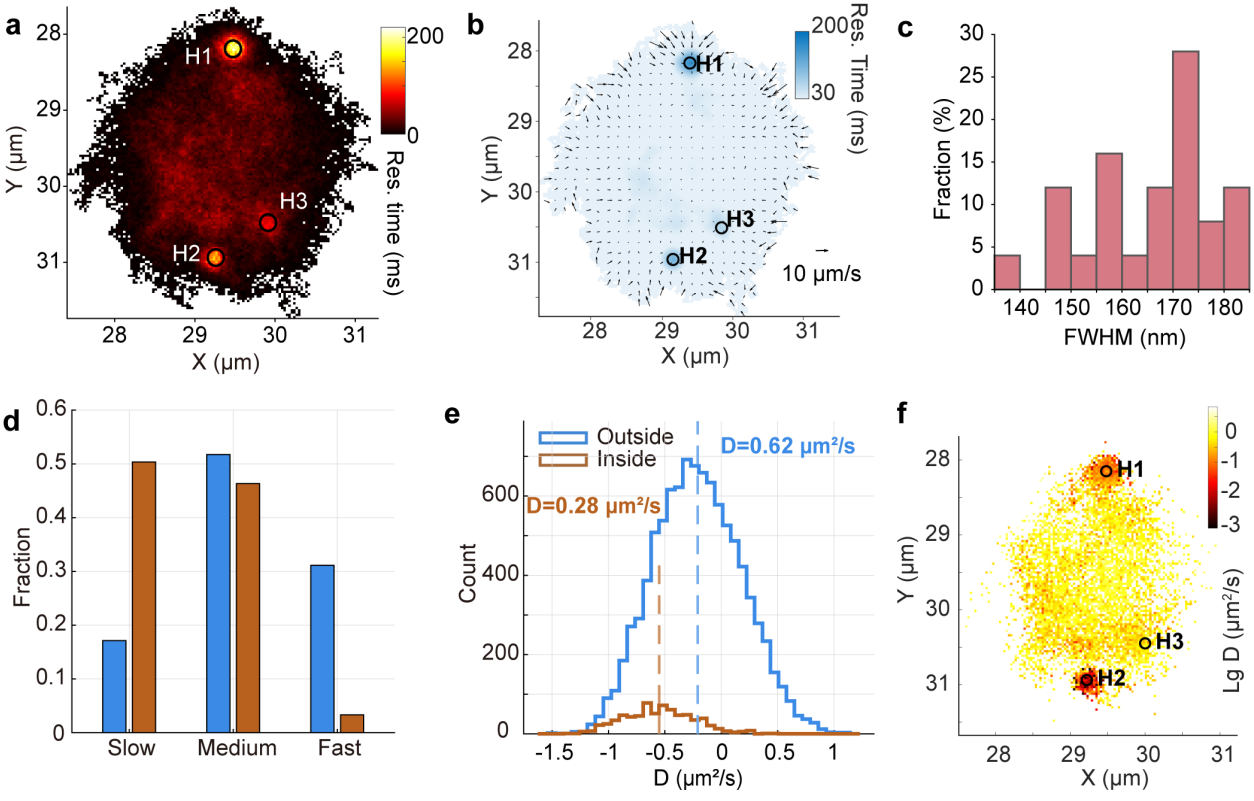

Figure 3. Residence hotspots identify locally slow environments within tau condensates. (**a**) Spatial residence map reconstructed from a long tau trajectory. Pixel size: 30 nm. H1–H3 denote representative localized high-residence regions. (**b**) Local drift field calculated from 20-ms lagged

displacements for the same trajectory and overlaid on the corresponding occupancy map. Arrows indicate the local mean displacement direction and reveal reproducible directional structure around the high-residence regions. Arrow length represents the magnitude of the local mean drift velocity; scale bar, 10 μm s^{-1}. (**c**) Distribution of hotspot sizes. Hotspots were fitted with two-dimensional Gaussian profiles and the fitted FWHM was used to estimate the apparent hotspot dimension. (**d**) Fractional occupancy of slow, intermediate, and fast HMM states inside and outside identified hotspots. Outside hotspots: slow, 0.17; medium, 0.52; fast, 0.31. Inside hotspots: slow, 0.50; medium, 0.46; fast, 0.03. (**e**) Distribution of apparent tau mobility inside and outside hotspots. (**f**) Spatial map of the apparent diffusion coefficient for the representative trajectory shown in (a). Each diffusion estimate was assigned to the mean molecular position sampled during the corresponding 10-ms fitting window and spatially averaged on a 30-nm grid. H1 and H2 coincide with regions of reduced local diffusivity, whereas H3 exhibits pronounced residence enrichment without a comparable decrease in apparent diffusivity, illustrating distinct local relationships between molecular occupancy and mobility. The temporal precision of trajectory used here is 100 μs.

The residence hotspots were fitted with two-dimensional Gaussian profiles to estimate their characteristic size. Across 75 analyzed trajectories, hotspot full widths at half maximum were predominantly in the approximate 0.13–0.19-μm range (**Fig. 3c**), indicating sub-condensate regions of enriched residence rather than whole-droplet confinement.

At the population level, hotspot-associated segments were kinetically distinct from the remaining portions of the trajectories. Across 75 trajectories, hotspot-associated segments showed a greater contribution from the slow mobility state and reduced contributions from intermediate and fast states compared with trajectory regions outside hotspots (**Fig. 3d and Supplementary Fig. 6**). Consistently, the distribution of apparent diffusion coefficients shifted toward lower mobility within hotspots (**Fig. 3e**).

Although residence hotspots were associated with reduced mobility at the population level, inspection of spatially resolved occupancy and diffusion within individual trajectories revealed a more heterogeneous relationship (**Fig. 3f**). In the representative trajectory, residence hotspots areas

H1 and H2 coincided with pronounced local reductions in diffusion coefficients, whereas H3 exhibited strong occupancy enrichment without a comparable decrease in diffusivity. Thus, enhanced residence and diffusional slowing were not strictly coupled across individual hotspots. Together, these observations suggest partially decoupled occupancy and kinetic landscapes within the condensate, indicating that local molecular enrichment can arise through distinct mechanisms, including diffusional confinement and preferential occupancy that is not accompanied by pronounced mobility reduction.

Together, these observations link spatial revisitation to reduced mobility within the history of the same molecule and support a model in which tau molecules dynamically sample localized subregions of stronger confinement or stronger interaction within the condensate interior[10]. Importantly, however, the current measurements show dynamic sampling of heterogeneous local environments; they do not by themselves establish whether those environments are fixed, slowly evolving or actively remodeling over the course of observation.

Long 3D trajectories reveal boundary-associated shell-like motion

Condensate interfaces can contribute additional kinetic resistance to molecular transport and may exhibit properties distinct from either bulk phase[38, 39]. We therefore examined long trajectories localized near the condensate boundary. In representative measurements, tau trajectories followed an extended shell-like path along the condensate periphery rather than sampling the entire enclosed volume isotropically (**Fig. 4a and Supplementary Fig. 7–9**). Projection of one such trajectory onto the imaging plane followed an approximately arc-shaped boundary with an apparent radius of approximately 0.97 μm (**Fig. 4b**). Local mobility along this path was predominantly low, and the two-dimensional residence maps recovered the same boundary-enriched geometry (**Fig. 4b,c**). A further boundary-associated trajectory showed qualitatively similar behavior (**Supplementary Fig. 9**). Moreover, we compared the mobility of this boundary-associated trajectory with a tau trajectory inside the same condensate (**Fig. 4d-f, Supplementary Fig. 8**). The apparent diffusion coefficient of tau near the condensate boundary was approximately two orders of magnitude lower than that within the condensate interior.

This finding shows that the motion of tau at or along a condensate boundary depends not only on bulk dense-phase viscosity but also on the structure and transport properties of the interface itself. In the present system, the shell-like trajectories suggest that tau can move along the

periphery in a restricted, interface-associated mode. That behaviour is consistent with the idea that the boundary contributes its own transport landscape, one that differs from both the condensate interior and the surrounding dilute phase, rather than being treated only as a geometric boundary[38, 39].

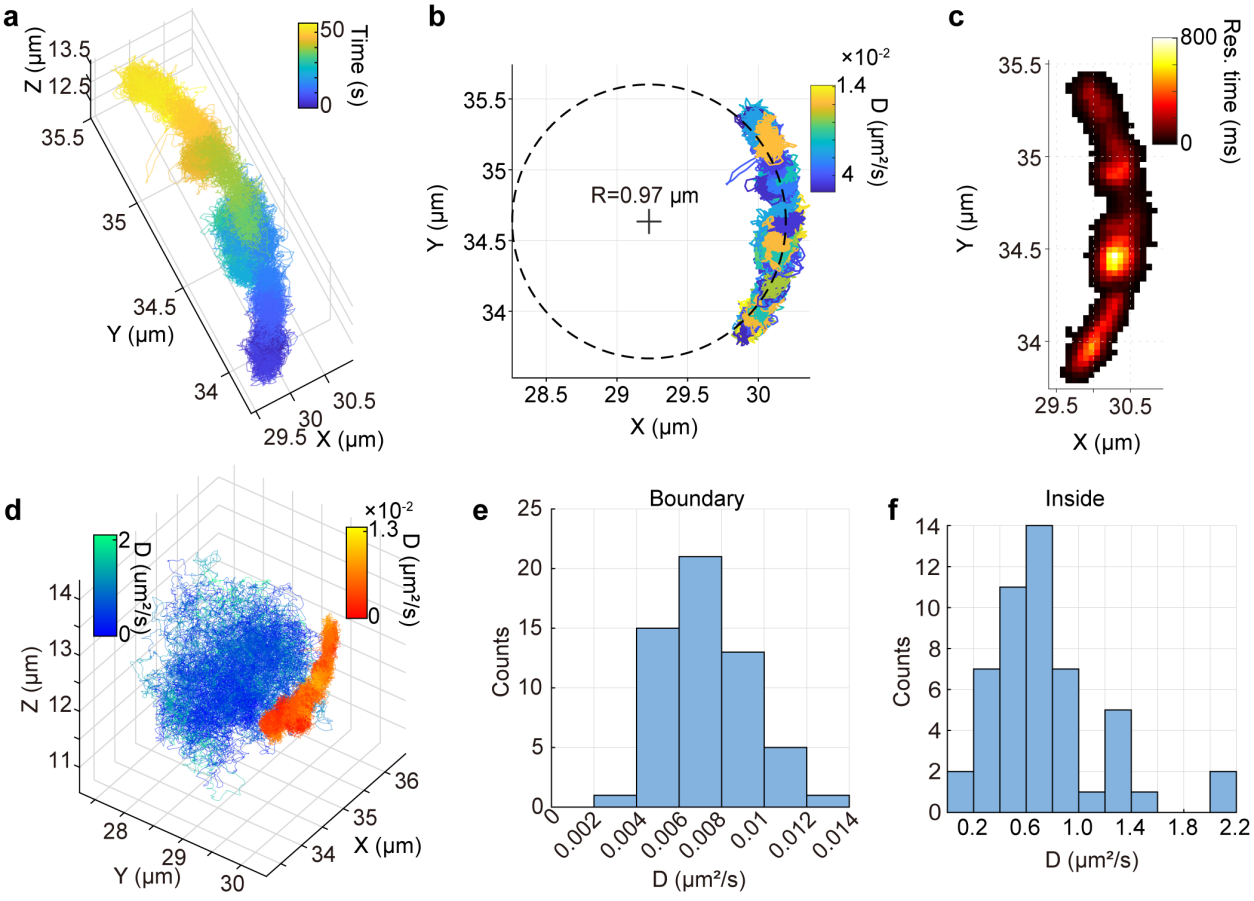

Figure 4. Long trajectories reveal shell-like boundary-associated tau motion with reduced mobility. (**a**) Representative three-dimensional tau trajectory near a condensate boundary. Color-coded by time. (**b**) Projection of the trajectory onto the XY plane, color-coded by local apparent mobility. Fitting yields an apparent shell radius of 0.97 μm. (**c**) Two-dimensional residence map reconstructed from the same trajectory, revealing boundary-enriched residence. (**d**) Three-dimensional trajectory of tau near the condensate boundary (red-to-yellow) and a tau trajectory within the same condensate interior (blue-to-green), color-coded by apparent diffusion coefficient. (**e**) Distribution of apparent diffusion coefficients for the boundary-associated trajectory. (**f**) Distribution of apparent diffusion coefficients for the interior trajectory.

Repeated inter-condensate transfer enables coarse-grained apparent free-energy analysis from a single trajectory

Direct observation of molecular transfer between adjacent condensates is challenging because conventional imaging typically captures only short temporal windows. The long-duration active-feedback 3D tracking enables the capture of these rare molecular exchange events. In a representative event, an individual tau molecule translocated between two neighboring condensates several times within one temporally continuous 46-s record (**Fig. 5 and Supplementary Fig. 10**). During this event, the apparent speed of the molecule increased in the inter-condensate region compared with the motion observed within either condensate (**Fig. 5c**). We infer that the two condensates are not completely separated but are partially connected, with the connecting region facilitating molecular transfer between them. An additional inter-condensate transfer event is shown in **Supplementary Fig. 11**.

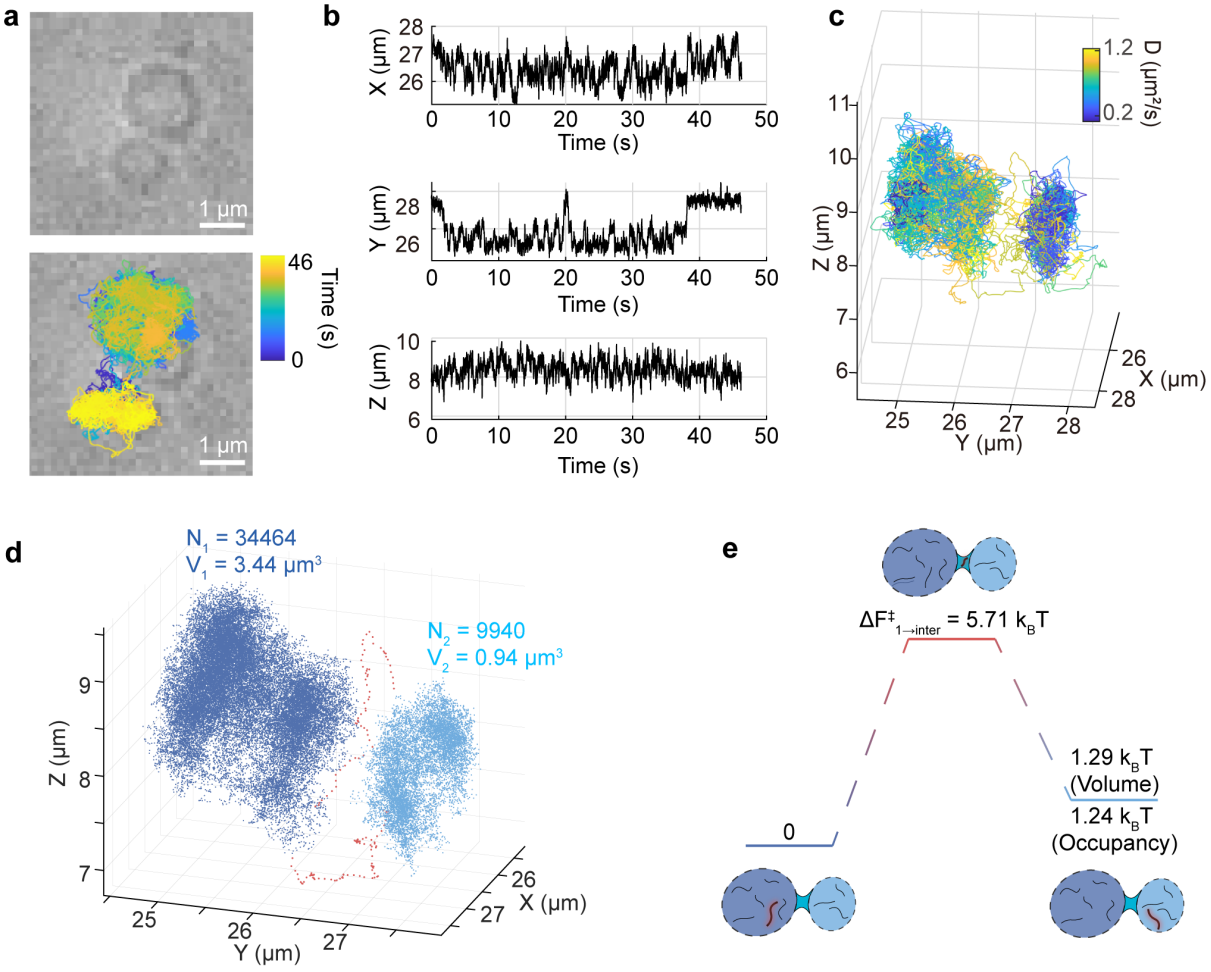

Figure 5. Repeated transfer between adjacent condensates enables trajectory-derived apparent free-energy analysis. (a) Bright-field image of two adjacent condensates (top) and the corresponding time-colored tau trajectory overlaid on the condensate pair (bottom). Scale bars: 1 μm. **(b)** x, y and z coordinates as a function of time for trajectory (**a**). **(c)** Three-dimensional trajectory of the same 46-s condensate-to-condensate transfer event, color-coded by apparent diffusion coefficient. (**d**) Three-dimension localization point clouds assigned to condensate-associated states 1 and 2 and to inter-condensate transition states, together with the corresponding numbers of localizations, N_i, and tau-accessible volumes, V_i. (**e**) Apparent free-energy diagram constructed from the relative occupancy of the trajectory-defined states, showing the free-energy difference between the two condensate-associated states and the apparent free-energy elevation associated with the inter-condensate transition state.

Importantly, the long observation window further allowed the trajectory to be segmented at 1-ms sampling interval into two condensate-associated states and an inter-condensate transition state (**Fig. 5d**, see also **Methods** for detailed information). Individual inter-condensate transitions were brief, with a median duration of only 16.5 ms, highlighting the high temporal resolution of 3D-SMART as a key requirement for directly resolving these transient molecular exchange events. In contrast, tau spent substantially longer periods confined within the two condensates, allowing the relative time spent in each condensate-associated state to be quantified as its fractional occupancy. The three-dimensional localization distributions assigned to each condensate-associated state were further used to estimate the accessible volume sampled by tau within each condensate, yielding 3.44 μm^3 and 0.94 μm^3 for condensates 1 and 2, respectively.

The relative partitioning of tau localizations among the trajectory-defined states encodes thermodynamic information that can be extracted. Based on Boltzmann's distribution, the energy difference between two condensates can be calculated,

$$F_i = -k_B T \ln \frac{N_i}{N_1 + N_2} + C,$$

$$\Delta F_{1-2} = F_2 - F_1 = -k_B T \ln \frac{N_2}{N_1},$$

where N_i is the number of 1-ms localizations assigned to condensate i. For the representative trajectory, this analysis gives

$$\Delta F_{1-2} = 1.24\, k_B T.$$

More importantly, the successful identification of the inter-condensate population makes it possible to compute the apparent free-energy elevation for leaving a condensate in a similar way:

$$\Delta F^{\ddagger}_{i\to inter} = -k_B T \ln \frac{N_{inter}}{N_i},$$

where N_{inter} is the number of localizations assigned to the inter-condensate transition state. The calculated apparent free-energy elevation for tau to leave condensate-associated state 1 is $5.71 k_B T$.

We next asked how much of the condensate-to-condensate free-energy difference could be accounted for by the difference in configurational space sampled by tau. Under a simple configurational model in which the local energetic environment experienced by tau is comparable between two condensates, the number of accessible spatial microstates, Ω_i, is expected to scale with tau-accessible volume, V_i. From Boltzmann's entropy formula $S_i = k_B \ln \Omega_i$, the corresponding configurational contribution to the free energy difference is therefore

$$\Delta F_{config,1-2} = -k_B T \ln \frac{V_2}{V_1}$$

where V_i is the accessible configurational volume of condensate i calculated from the three-dimensional configurational space sampled by tau (see **Methods** for detailed information). The calculated free-energy difference from condensate geometry is $1.29\ k_B T$, which is in close agreement with the free-energy difference computed from the occupancy ($1.24 k_B T$). Thus, the asymmetry in molecular occupancy observed in this event is quantitatively consistent with the difference in configurational space sampled by tau within the two condensate-associated states (**Fig. 5e**).

Together, these measurements demonstrate that long-term active-feedback 3D tracking not only provides a direct single-molecule view of condensate exchange but also allows the extraction of a coarse-grained apparent free-energy landscape from individual trajectories. The same trajectory simultaneously reports molecular mobility, confinement, state occupancy, state

transitions, and accessible configurational space, enabling molecular exchange and partitioning to be examined within one continuous single-molecule history, which is unattainable through ensemble measurement.

Discussion

The movement of a biomolecule through a condensate can be revealed by its trajectory: a molecule can encounter local environments, remain confined, escape, revisit previous regions, approach an interface and transfer to another phase or condensate. Preserving that temporal sequence is therefore essential if molecular transport is to be understood as a continuous physical process rather than as a collection of disconnected displacement measurements. Here, we utilized active-feedback 3D tracking to preserve this sequence over long observation periods. In reconstituted tau condensates, continuous long trajectories revealed recurrent switching among three mobility states, spatially localized residence hotspots, prolonged boundary-associated motion and single-molecule translocation between neighboring condensates. In the representative inter-condensate trajectory, the long observation window together with high spatiotemporal precision enabled a coarse-grained apparent free-energy analysis derived from state occupancy and molecule-accessible volume. The close agreement between occupancy- and volume-derived estimates illustrates how a continuous single-molecule trajectory can relate molecular partitioning to the configurational space explored by the molecule. Together, these observations support a picture in which the dense phase acts as a heterogeneous transport landscape rather than as a spatially uniform medium characterized by a single effective diffusion coefficient.

More broadly, this work establishes long-term real-time 3D single-molecule tracking as a dynamic nanometrology approach for condensate research. The approach complements ensemble exchange measurements and static structural readouts by preserving the time-ordered motion history of individual molecules. Future combinations with controlled perturbations, interfacial physical analysis and orthogonal structural measurements should help define the physical origin of the microenvironments resolved here. Extending the platform to simultaneous fluorescence-anisotropy or fluorescence-lifetime measurements would enable simultaneous measurement of protein conformational information and positional dynamics within condensates[40, 41]. Such multidimensional measurements could ultimately reveal how molecular conformation, interactions, and mesoscale condensate organization evolve together in real time.

Methods

Expression and purification of recombinant tau protein

Recombinant tau protein was expressed in *Escherichia coli* BL21(DE3) cells (Vazyme, C504) carrying the pT7-6×His-tau plasmid. Cells were grown in LB broth medium (Sangon Biotech, A507002) supplemented with kanamycin sulfate (50 μg/mL; Macklin, K812217). Protein expression was induced with 1 mM isopropyl β-D-1-thiogalactopyranoside (IPTG; Macklin, I885106) when the OD600 reached 0.8–1.0. Protein expression was then allowed to proceed overnight at 18 °C in a temperature-controlled shaking incubator (Shanghai Zhichu, ZQZY-78BE). Cells were harvested by centrifugation at 8000 g for 10 min at 4 °C using a high-speed centrifuge (Beckman Coulter, J-26S XP), and the pellets were stored at -80 °C until purification.

Tau protein was purified by Ni^{2+}-affinity chromatography followed by anion-exchange chromatography. Bacterial pellets were resuspended in lysis buffer containing 50 mM Tris-HCl (Beyotime, ST786), 100 mM NaCl (Sangon Biotech, A100241), and 1 mM PMSF (Servicebio, G2008), pH 8.0, and lysed by high-pressure homogenization using a high-pressure homogenizer (ATS, AH-NANO) at 800 bar. The lysate was clarified by centrifugation at 30,000 rpm for 45 min at 4 °C using an ultracentrifuge (Beckman Coulter, Optima XPN-100), and then filtered through a 0.22 μm PES membrane (Bioleader, BS635003) before chromatographic purification.

His-tagged tau was first purified using a HisTrap HP column (Cytiva, 17524801) on an ÄKTA purification system (Cytiva, ÄKTA Pure 150 M3) and eluted with an imidazole gradient. Tau-containing fractions were pooled, concentrated, and further purified by anion-exchange chromatography using a HiTrap Q HP column (Cytiva, 29018182) with a NaCl gradient.

Eluted fractions were analyzed by SDS-PAGE using a 12% PAGE gel preparation kit (Servicebio, 4693132001), and protein bands were visualized by Coomassie Brilliant Blue staining (Yeasen, 20308ES72). Tau identity was further confirmed by Western blotting. Fractions corresponding to the tau elution peak were pooled and dialyzed overnight at 4 °C against storage buffer containing 50 mM Tris-HCl, 500 mM NaCl, 1 mM DTT (Solarbio, D1070), 1 mM EDTA (Beyotime, ST066), and 20% glycerol (Sangon Biotech, A501745). Protein concentration was determined using a

Bradford protein assay kit (Biosharp, BL524A). Purified tau protein was aliquoted, snap-frozen in liquid nitrogen, and stored at -80 °C.

Fluorescent labelling of tau

Tau protein was buffer exchanged into 0.1 M sodium bicarbonate buffer (pH 8.3; Aladdin, S5761), using centrifugal filters (Merck Millipore, UFC5030). SeTau647-NHS ester (SETA Biomedicals, K9-4149) was added at a dye-to-protein molar ratio of 10:1, and the reaction was performed at 4 °C for 3 h in the dark. Free dye was removed using a desalting column (Thermo Fisher Scientific, 89882). The concentration of labeled tau and the dye-to-protein ratio were determined by measuring absorbance at 280 nm and at the dye absorption maximum, with correction for dye contribution at 280 nm. Labeled tau was aliquoted and stored at -80 °C in the dark.

In vitro reconstitution of tau condensates

Unlabeled tau and SeTau647-labeled tau were mixed at a molar ratio of 19:1 for the confocal imaging experiment. The protein mixture was diluted into phase-separation buffer containing 50 mM Tris-HCl, 1 mM DTT, 1 mM EDTA, and 10% (w/v) PEG 8000 (BioSharp, BS138), pH 7.4, with NaCl concentrations adjusted to 10, 50, or 150 mM. The final tau concentrations were 2, 5, or 10 μM. Samples were gently mixed and incubated at room temperature (25 °C) for 10 min to allow condensate formation.

Turbidity assay

Tau condensate formation was monitored by turbidity at 600 nm. Samples prepared as described above were transferred to a 96-well plate (Sangon Biotech, F605033), and OD600 was measured at 37 °C using a microplate reader (SCILOGEX, SCI-VS). Samples were shaken for 10 s before each measurement, and OD600 values were recorded every 5 min for 3 h. For each sample, three readings were collected and averaged.

Confocal fluorescence microscopy

Tau condensates were imaged using a confocal microscope (ZEISS, LSM 980) equipped with a 63×/1.40 NA oil-immersion objective. SeTau647 was excited with a 640 nm laser, and fluorescence emission was collected at 650–750 nm. Images were acquired at 1024 × 1024 pixels with the pinhole set to 1 Airy unit. For comparable samples, the laser power was set to 0.5%, and

the detector gain was kept at 550. Time-lapse images were acquired every 0.13 s for 1 min when condensate dynamics were recorded.

FRAP assay

FRAP experiments were performed using tau condensates prepared as described above. Condensates with clear boundaries and low background fluorescence were selected for bleaching. Images were acquired at 256 × 256 pixels to improve temporal resolution. A circular region of interest (ROI) with a radius of 0.2 μm was selected within the condensate, and a background region of the same size was selected outside the condensate. Five pre-bleach images were collected before photobleaching. The selected ROI was then bleached using a 405 nm laser at 100% power for 50 iterations. After bleaching, fluorescence recovery was recorded using a 640 nm laser at 0.5% power. Fluorescence intensity was corrected for background and normalized, and recovery curves were fitted with a single-exponential recovery model to obtain the half-recovery time ($t_{1/2}$).

Sample preparation for single-molecule tracking

Glass coverslips (Marienfeld, NO.1.5H) were passivated before tracking experiments to reduce tau adsorption and condensate wetting on the glass surface. Coverslips were sonicated in 1 M NaOH (Aladdin, S431791) for 1 h, thoroughly rinsed with deionized water, and sonicated in anhydrous ethanol (Hushi, 10009218) for another 1 h. After drying, the coverslips were treated with Sigmacote (Aladdin, 41116121) for 3 min, followed by incubation with 1% (w/v) pluronic F-127 (Beyotime, ST501) for 1 h. The treated coverslips were then assembled into metal imaging chambers before sample loading.

For single-molecule tracking, tau condensates were prepared with a very low fraction of fluorescently labeled tau to minimize the probability of multiple fluorophores entering the excitation volume simultaneously. Unlabeled tau and SeTau647-labeled tau were mixed at a molar ratio of 99,999:1 and diluted into phase-separation buffer to a final tau concentration of 5 μM. The NaCl concentration was set to 10 mM for tracking experiments. The sample was gently mixed, immediately transferred into the passivated imaging chamber, and incubated at room temperature in the dark for 10 min before tracking.

Active-feedback 3D single-molecule tracking

Long-duration 3D single-molecule tracking was performed on a previously developed 3D-SMART platform. A 638 nm laser (LBX-638-100-CSB-PPA, OXXIUS) was used for excitation. A tunable acoustic gradient lens (TAGLENS-T1, Mitutoyo) provided rapid axial modulation and two-dimensional electro-optic deflectors (Model 310A, Conoptics Inc.) generated lateral beam steering, together producing a three-dimensional excitation pattern around the target fluorophore. The excitation beam was focused onto the sample through a 100×/1.40 NA oil-immersion objective (HC PL APO 100×/1.40 OIL CS2, Leica). The excitation and emission light was separated by a dichroic mirror (ZT405/488/561/640 rpcv2, Chroma). Photon arrival times were recorded on a single-photon detector (SPCM-AQRH-15, Excelitas) and processed in real time by FPGA (PCIe-7858, National Instruments Corp.) to estimate molecular position. The estimated position was fed back to a nanopositioning stage (Nano-PDQ275 and Nano-OPQ65, Mad City Lab) to maintain the tracked molecule near the center of the excitation volume. Instrument hardware and active-feedback logic followed previously described implementations of real-time 3D single-molecule tracking. The position of the piezo nanopositioning stage was used to reconstruct the molecule's 3D trajectory at a temporal resolution of 1 ms, unless otherwise specified. For trajectories reconstructed using recursive Bayesian estimation, a temporal resolution of 100 μs was achieved.

For tau single-molecule tracking, the imaging chamber containing tau condensate samples was placed on the microscope stage. SeTau647 was excited with the 638 nm laser at a power of approximately 2 μW before the objective. Before tracking, the laser spot position was recorded, and a bright-field image of the target condensate was acquired for spatial alignment. A condensate with clear morphology was selected, and the laser spot was positioned within the condensate. Tracking was initiated automatically when a fluorescent tau molecule entered the excitation volume and the APD photon count rate exceeded the preset threshold.

Contributions

S.H. initiated, conceived, and supervised the project. J.H. and R.L. conducted the experiments and analyzed the data. Y.L. performed the data analysis. Z.S and Y.T. performed the recursive Bayesian reconstruction. S.H., J. H., R. L., and Y. L. wrote the manuscript.

Acknowledgement

We would like to acknowledge the funding support from National Natural Science Foundation of China (22574109) and Major Program of Shenzhen Bay Laboratory (C1012524004).

Competing interests

The authors declare no conflicts of interest.

Data availability.

The data underlying the findings of this study will be deposited in Zenodo and made publicly available upon publication.

References

1. Lyon, A.S., Peeples, W.B. & Rosen, M.K. A framework for understanding the functions of biomolecular condensates across scales. *Nature Reviews Molecular Cell Biology* **22**, 215-235 (2021).
2. Alberti, S. et al. Current practices in the study of biomolecular condensates: a community comment. *Nature Communications* **16**, 7730 (2025).
3. Pei, G., Lyons, H., Li, P. & Sabari, B.R. Transcription regulation by biomolecular condensates. *Nature Reviews Molecular Cell Biology* **26**, 213-236 (2025).
4. Nandana, V. & Schrader, J.M. Roles of liquid–liquid phase separation in bacterial RNA metabolism. *Current Opinion in Microbiology* **61**, 91-98 (2021).
5. Jaqaman, K. & Ditlev, J.A. Biomolecular condensates in membrane receptor signaling. *Current Opinion in Cell Biology* **69**, 48-54 (2021).
6. Alberti, S. & Hyman, A.A. Biomolecular condensates at the nexus of cellular stress, protein aggregation disease and ageing. *Nature Reviews Molecular Cell Biology* **22**, 196-213 (2021).
7. Silva, J.L. et al. Targeting Biomolecular Condensation and Protein Aggregation against Cancer. *Chemical Reviews* **123**, 9094-9138 (2023).
8. Mathieu, C., Pappu, R.V. & Taylor, J.P. Beyond aggregation: Pathological phase transitions in neurodegenerative disease. *Science* **370**, 56-60 (2020).
9. Sumrall, E.R., Husna, S.M.A., Halder, B., Ahnoud, A. & Walter, N.G. Single-molecule microscopy of biomolecular condensates: From liquid droplets to heterogeneous networks. *Current Opinion in Structural Biology* **98**, 103271 (2026).
10. Shen, Z. et al. Biological condensates form percolated networks with molecular motion properties distinctly different from dilute solutions. *eLife* **12**, e81907 (2023).
11. Liao, Z. et al. Emergent mechanics of a networked multivalent protein condensate. *Nature Communications* **16**, 5237 (2025).
12. Gao, G., Sumrall, E.R. & Walter, N.G. Nanoscale domains govern local diffusion and ageing within fused-in-sarcoma condensates. *Nature Nanotechnology* **21**, 249-258 (2026).

13. Wu, T. et al. Single-fluorogen imaging reveals distinct environmental and structural features of biomolecular condensates. *Nature Physics* **21**, 778-786 (2025).
14. Dar, F. et al. Biomolecular condensates form spatially inhomogeneous network fluids. *Nature Communications* **15**, 3413 (2024).
15. Chin Sang, C., Upadhyay, S., Nosella, M.L., Forman-Kay, J.D. & Lee, H.O. The dynamic and heterogeneous composition of biomolecular condensates and its functional relevance. *Nature Reviews Molecular Cell Biology* **27**, 278-296 (2026).
16. Ye, S. et al. Micropolarity governs the structural organization of biomolecular condensates. *Nature Chemical Biology* **20**, 443-451 (2024).
17. Zhang, X., Li, H., Ma, Y., Zhong, D. & Hou, S. Study liquid–liquid phase separation with optical microscopy: A methodology review. *APL Bioengineering* **7** (2023).
18. Garcia, P.L., Chakravarti, A. & Joseph, J.A. Progress toward linking single-molecule behavior and condensate material properties. *Current Opinion in Structural Biology* **100**, 103323 (2026).
19. Taylor, N.O., Wei, M.-T., Stone, H.A. & Brangwynne, C.P. Quantifying Dynamics in Phase-Separated Condensates Using Fluorescence Recovery after Photobleaching. *Biophysical Journal* **117**, 1285-1300 (2019).
20. Brangwynne, C.P. et al. Germline P Granules Are Liquid Droplets That Localize by Controlled Dissolution/Condensation. *Science* **324**, 1729-1732 (2009).
21. Beutel, O., Maraspini, R., Pombo-García, K., Martin-Lemaitre, C. & Honigmann, A. Phase Separation of Zonula Occludens Proteins Drives Formation of Tight Junctions. *Cell* **179**, 923-936.e911 (2019).
22. Jawerth, L. et al. Protein condensates as aging Maxwell fluids. *Science* **370**, 1317-1323 (2020).
23. Alshareedah, I., Moosa, M.M., Pham, M., Potoyan, D.A. & Banerjee, P.R. Programmable viscoelasticity in protein-RNA condensates with disordered sticker-spacer polypeptides. *Nature Communications* **12**, 6620 (2021).
24. Costa, L., Li-Destri, G., Pontoni, D., Konovalov, O. & Thomson, N.H. Liquid–Liquid Interfacial Imaging Using Atomic Force Microscopy. *Advanced Materials Interfaces* **4**, 1700203 (2017).
25. Ramat, A., Haidar, A., Garret, C. & Simonelig, M. Spatial organization of translation and translational repression in two phases of germ granules. *Nature Communications* **15**, 8020 (2024).
26. He, C., Wu, C.Y., Li, W. & Xu, K. Multidimensional Super-Resolution Microscopy Unveils Nanoscale Surface Aggregates in the Aging of FUS Condensates. *Journal of the American Chemical Society* **145**, 24240-24248 (2023).
27. Bo, S., Hubatsch, L. & Jülicher, F. Single-molecule trajectories of reactants in chemically active biomolecular condensates. *arXiv preprint arXiv:2503.19517* (2025).
28. Hou, S., Exell, J. & Welsher, K. Real-time 3D single molecule tracking. *Nature Communications* **11**, 3607 (2020).
29. Tan, X. et al. Active-Feedback 3D Single-Molecule Tracking Using a Fast-Responding Galvo Scanning Mirror. *The Journal of Physical Chemistry A* **127**, 6320-6328 (2023).
30. Sha, H. et al. Single molecule spectrum dynamics imaging with 3D target-locking tracking. *Nature Communications* **16**, 8686 (2025).

31. Lin, Y., Lin, H. & Welsher, K.D. Super-Resolving Particle Diffusion Heterogeneity in Porous Hydrogels via High-Speed 3D Active-Feedback Single-Particle Tracking Microscopy. *Small* **21**, e05319 (2025).
32. Lin, Y., Exell, J., Lin, H., Zhang, C. & Welsher, K.D. Hour-Long, Kilohertz Sampling Rate Three-Dimensional Single-Virus Tracking in Live Cells Enabled by StayGold Fluorescent Protein Fusions. *The Journal of Physical Chemistry B* **128**, 5590-5600 (2024).
33. Ambadipudi, S., Biernat, J., Riedel, D., Mandelkow, E. & Zweckstetter, M. Liquid–liquid phase separation of the microtubule-binding repeats of the Alzheimer-related protein Tau. *Nature Communications* **8**, 275 (2017).
34. Kanaan, N.M., Hamel, C., Grabinski, T. & Combs, B. Liquid-liquid phase separation induces pathogenic tau conformations in vitro. *Nature Communications* **11**, 2809 (2020).
35. Donnert, G., Eggeling, C. & Hell, S.W. Major signal increase in fluorescence microscopy through dark-state relaxation. *Nature Methods* **4**, 81-86 (2007).
36. Boudreau, C. et al. Excitation Light Dose Engineering to Reduce Photo-bleaching and Photo-toxicity. *Scientific Reports* **6**, 30892 (2016).
37. Hou, S., Zhang, C., Niver, A. & Welsher, K.D. Mapping Nanoscale Forces and Potentials in Live Cells with Microsecond 3D Single-Particle Tracking. *Chemical & Biomedical Imaging* (2026).
38. Zhang, Y. et al. The exchange dynamics of biomolecular condensates. *eLife* **12**, RP91680 (2024).
39. Hubatsch, L. et al. Transport kinetics across interfaces between coexisting liquid phases. *eLife* **14**, RP106842 (2025).
40. Manger, L.H. et al. Revealing Conformational Variants of Solution-Phase Intrinsically Disordered Tau Protein at the Single-Molecule Level. *Angewandte Chemie* **129**, 15790-15794 (2017).
41. Foote, A.K., Manger, L.H., Holden, M.R., Margittai, M. & Goldsmith, R.H. Time-resolved multirotational dynamics of single solution-phase tau proteins reveals details of conformational variation. *Physical Chemistry Chemical Physics* **21**, 1863-1871 (2019).